



Seismic behavior of earthquake-damaged hybrid connections reinforced with replaceable energy-dissipating elements

Tianyang Zhang^a, Weizhi Xu^{a,b,*}, Shuguang Wang^a, Dongsheng Du^a, Linlin Xie^b, Qisong Miao^c

^a College of Civil Engineering, Nanjing Tech University, Nanjing, China

^b Multi-Functional Shaking Tables Laboratory, Beijing University of Civil Engineering and Architecture, Beijing, China

^c Beijing Institute of Architectural Design, Beijing, China

ARTICLE INFO

Keywords:

Earthquake damage
Unbonded post-tensioned prestress
Reinforcing
Replaceable energy-dissipating elements
Seismic behavior

ABSTRACT

In recent years, self-centering post-tensioned concrete structures have received extensive research attention owing to their excellent seismic performance and post-earthquake functional recoverability. This study entailed the development of a novel repair method for earthquake-damaged unbonded post-tensioned hybrid connections (PTHCs) by using a novel energy-dissipating device to improve seismic resilience. To investigate the effectiveness of the repair method, four connections with different degrees of seismic damage were repaired using different repair methods, and quasi-static experiments were then conducted. The test variables included the position of the glass fiber-reinforced polymer (GFRP) arrangement, connection method of energy-dissipating devices, number of replaceable energy-dissipating elements (REDEs) of the damper, and initial prestressing force of post-tensioned (PT) strands. The experimental results indicate that the proposed repair methods can recover the lost capacities of PTHCs, and the mechanical properties of the reinforced self-centering precast connections (RSCPCs) can even be restored by replacing the REDEs under a second rare earthquake. The proposed energy-dissipating device facilitates increase or decrease of the REDEs to meet the energy dissipation and stiffness targets of the component for different levels of earthquake damage. The calculation results based on the recovery force model were in good agreement with the test results, showing that the proposed model could reasonably predict the hysteresis behavior of the RSCPCs.

1. Introduction

A prefabricated concrete frame structure refers to a concrete structure assembled using precast concrete (PC) components through various reliable connection methods, including assembled monolithic concrete structures and fully assembled concrete structures. Compared with traditional reinforced concrete (RC) structures, PC structures have the advantages of high industrialization level, reducing the amount of wet work, reducing material consumption, and conforming to a carbon-neutral concept. In China, the process of industrialization is accelerating, and PC structures are emerging. Experimental studies [1–3] and post-earthquake field research [4–6] have shown that the poor ductility of connections is the main cause of structural damage in buildings. Therefore, connections between components become critical to ensure the integrity of PC structures.

To improve the seismic performance of PC structures, various connections have been developed and researched in recent decades.

* Corresponding author. College of Civil Engineering, Nanjing Tech University, Nanjing, China.

E-mail address: xuwz@njtech.edu.cn (W. Xu).

Post-tensioned (PT) prestressed structures provide self-centering capability through PT strands with less residual deformation in the connection regions and are therefore widely researched. In the 1990s, Precast Structural Seismic Systems (PRESSS) program was constituted to meet the resilience requirements of seismic design through collaborations between the United States and Japan [7–9]. Numerous scholars have studied the seismic performance and design methods for PT connections [10–14]. In 1995, Stone et al. [15] conducted experimental studies of four different hybrid connections to investigate the effect of different combinations of mild steel and PT strands, considering the test variable of whether the mild steel and PT strands inside the joint were bonded. Experimental studies showed that specimens with unbonded PT strands and unbonded mild steel exhibited the same or better performance as RC frame connections. Based on the experimental results of three 1/3-scale hybrid PC beam-to-column connections, Cheok et al. [13,16] proposed a hybrid connection design procedure that considers the mechanical behavior and hysteretic state of pre-embedded unbonded mild steel. Stanton et al. [17] performed a low-cycle reciprocal test on four hybrid connections, and the results demonstrated that the hybrid system had a large drift capacity and the same flexural strength as the RC system. Priestley et al. [18] conducted a pseudo-dynamic test on a five-story PC structure at a scale of 2/3. The structure consisted of four types of PC ductile connections and was subjected to a loading of 4.5 % drift ratio. The experiment demonstrated that the damage and residual deformation of the overall frame after the use of hybrid connections were lower than cast-in-place structures.

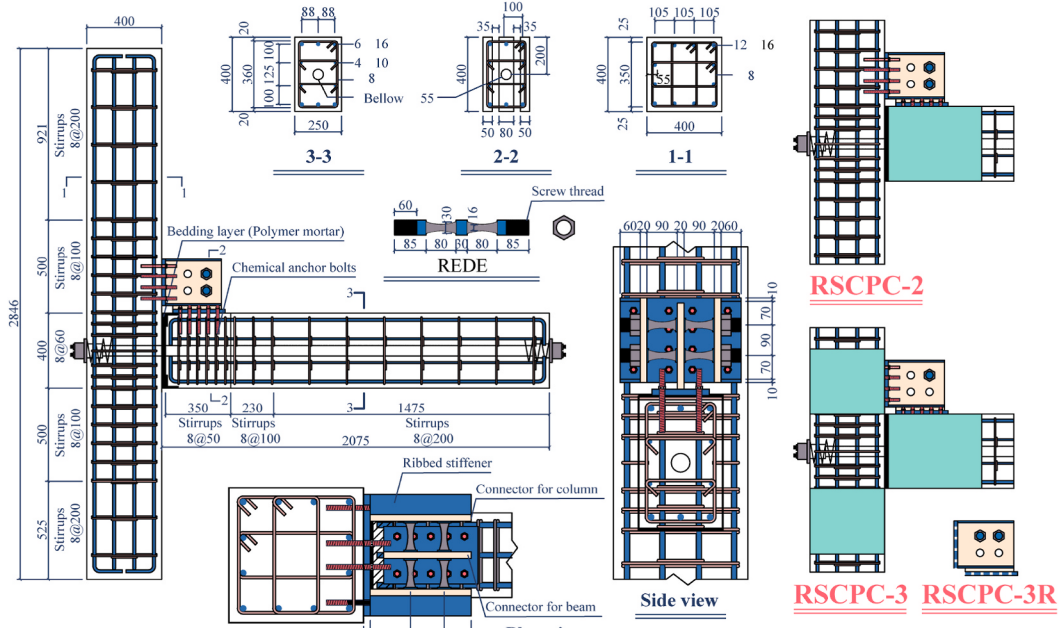
In the last two decades, post-tensioned PC beam-to-column connections have been extensively studied, inspired by the PRESSS research program. Ozden et al. [19] conducted hysteresis tests on five PT self-centering connections, and the research variables were mainly the contribution ratio of the pre-embedded energy-dissipating mild steel to the flexural capacity of the hybrid connections. The test results showed that a 20 %–30 % contribution to flexural strength was the most reasonable design. Based on the disadvantage of the weak energy-dissipating capability of PT connections, Morgen et al. [20,21] proposed friction dampers placed in the rotation area of the connections. Through a hysteresis experiment and finite element (FE) analysis, the novel connections were found to have less damage at large drifts, and the proposed structure exhibited good restoring properties. Takeaki [22] reported that the installation position of the friction device has a significant impact on the moment and energy-dissipating capacity of PT connections. Although the residual deformation of the friction damper-reinforced PT connections was small, the dampers provided less improvement in the load-carrying capacity of the beam end, and the side effects of the loss of the screw preload on the connections cannot be ignored.

Since the concept of seismic resilience design was proposed [23] and introduced to civil engineering [24–26], self-centering and low-damage structures have become a research hotspot. There has been a proliferation of research on PT structures, mainly focusing on steel damper reinforcing energy-dissipating connections [27–36]. Li et al. [30,37,38] proposed low-damage self-centering PC frame connections with replaceable dampers, which are a major advantage for this type of connections owing to their flexible expandability and replaceability. Liu et al. [34,39] utilized bamboo-shaped energy dissipaters to enhance the self-resetting connections, and their experimental results showed that the specimen under repeated loading possessed almost the same strength as the original connections. Wang et al. [33,40–42] used external unbonded mild steel bars to dissipate energy, thus overcoming the non-replaceability of hybrid connections in the PRESSS program. In the experiment, the beam ends adjacent to the column were reinforced by a steel jacket to constrain the concrete; however, diffuse cracking appeared outside the jacket. The bearing capacity and energy-dissipation efficiency of the hybrid connections were significantly degraded under large deformations, and the concrete fell locally. A series of explorations of external dampers for self-centering structures and reciprocating tests were conducted by Pampanin et al. [43–47]. The test results showed that the energy dissipaters can effectively contribute stiffness and energy dissipation capacity for the structures, and the damped self-centering structures had excellent seismic behaviour with very little residual damage.

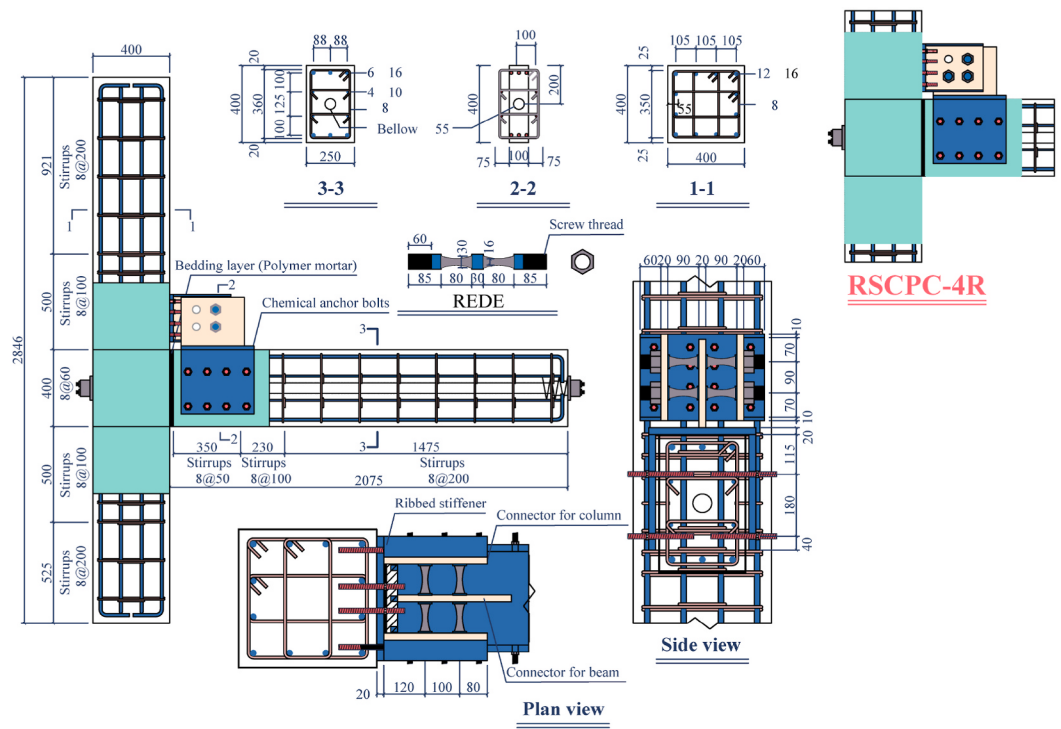
Previous studies have shown that GFRP reinforcement can improve the bearing capacity and stiffness of earthquake-damaged connections and that the repair methods for hybrid connections are borrowed from other structures [48–53]. The seismic damage of PTHCs is different from that of cast-in-place and external energy-dissipating connections because the energy-dissipating elements are embedded in the columns and beams. Most of the energy-dissipating parts of the hybrid connections were damaged inside the concrete, and some of the beam ends were damaged after the earthquake [54]. Therefore, it is necessary to conduct investigations focusing on the seismic reinforcing of these PTHCs.



Fig. 1. Damage status of PTHC specimens [54].

**RSCPC-1**

(a) RSCPC-1—RSCPC-3

**RSCPC-4**

(b) RSCPC-4

Fig. 2. Design details of all RSCPC connections.

2. Experimental program

The authors conducted experimental work on such PTHCs in the early stages [54] and typical damage modes of PTHCs are shown in Fig. 1. The proposed reinforced self-centering precast connections (RSCPCs) are based on the PTHCs after simulated earthquake damage, and the external energy-dissipating device from connectors to replaceable energy-dissipating elements (REDEs) are fully assembled. To verify the restoration effect of the structure after earthquake damage, the loading protocol and boundary constraint methods used in this study were the essentially same as those in the pre-experiment [54].

2.1. Specimen description

In general, four repaired and reinforced specimens were designed and tested, and the test variables included the location of the GFRP arrangement, the connection mode of energy-dissipating device, the number of REDEs and the prestress PT force. The column sections of all the specimens were 400 mm × 400 mm, and the beam sections were 250 mm × 400 mm. The height of all the columns was 2846 mm, the ratio of internal longitudinal reinforcement was 1.51 %, and all beams had a length of 2075 mm and a longitudinal reinforcement ratio of 0.60 %.

The beam ends of PTHC-1 and PTHC-2 were not adequately restrained in the previous tests, resulting in extensive diffuse cracking of the concrete at the beam end near the beam-column interface. Therefore, for these two specimens, a high-strength grouting material with a compressive strength of 80 MPa was used for extensive repairs. On the contrary, the concrete damage in PTHC-3 and PTHC-4 was minimal, with the main damage concentrated in the bedding layer at the interface of the beam and column. In this case, the use of a high-tenacity polymer mortar to repair the bedding layer was beneficial in reducing the loss of prestress during the experiment. To investigate the reinforcement constraint effect of glass fiber-reinforced polymer (GFRP) on the connections. No restrained reinforcement was applied to RSCPC-1, only the concrete at the beam end of RSCPC-2 was restrained, and the beam end adjacent to the column and part of the column area of RSCPC-3 was restrained, as shown in Fig. 2(a). Meanwhile, the core area of the column of RSCPC-4 was also reinforced, as shown in Fig. 2(b).

According to the hole position of the damper connectors, holes having a diameter of 18 mm and depth of 130 mm were drilled on the members, and a chemical anchor bolt with a diameter of 16 mm was implanted. The connectors of RSCPC-1–RSCPC-3 were detachable, as shown in Fig. 3(a), and the connector for the beam of RSCPC-4 was nondetachable, as shown in Fig. 3(b). Except for RSCPC-3, the specimens were installed with two initial REDEs. If no evident damage occurred to the beam-to-column connections at the end of loading, the REDEs, such as RSCPC-3R and RSCPC-4R, were replaced and reloaded. All the REDEs were threaded at both ends and connected to the connector using M 40 bolts. The reinforcement strategy for the PTHC specimen is illustrated in Fig. 4.

The prestressing tendons for all specimens were composed of four strands of 15.2 mm nominal diameter, with an equivalent area of 560 mm². The initial PT force was set at 281 kN for all specimens, except for the repeatedly loaded specimens RSCPC-3R and RSCPC-4R, where the initial PT force was set at 361 kN. The design parameters of the RSCPC specimens are presented in Table 1. By repairing and reinforcing the PTHCs, renamed RSCPCs, the earthquake-damaged PTHCs were used as the basis for the repair experiment [54].

2.2. Material properties

The compressive strength of the grout for the large-area repair was 80 MPa, and the nominal peak stress of the bedding repair polymer mortar was 50 MPa. The longitudinal reinforcements in all the specimens were recognized as HRB 400 with a yield strength of 437 MPa. The ultimate strength of the PT strands was 1857 MPa, and the chemical anchor bolt was composed of 304 stainless steel with a yield strength of 537 MPa. The nominal yield strengths of the steel used for the damper connectors and REDEs were 345 MPa and 235 MPa, respectively. The tensile strength of GFRP used in the reinforcement was 3700 MPa and the elongation at break was 4.3 %.

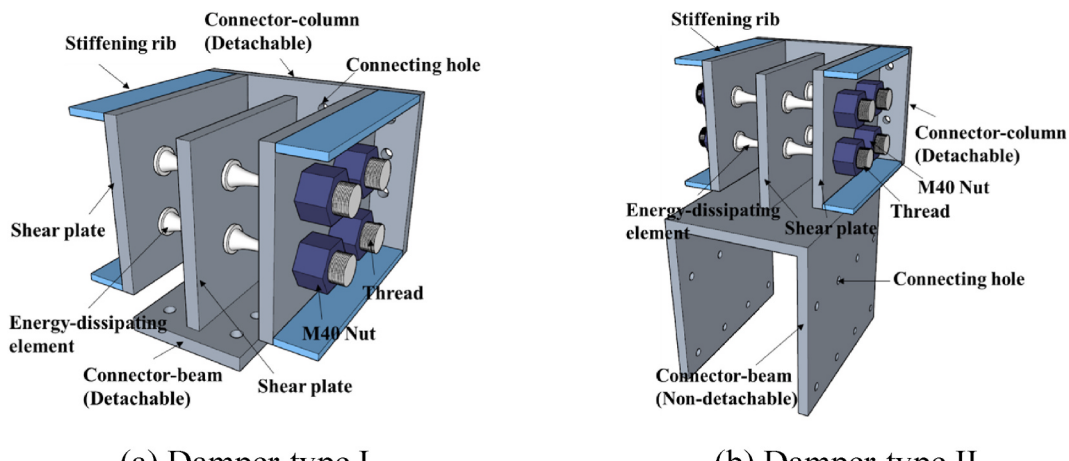


Fig. 3. Construction of the dampers.

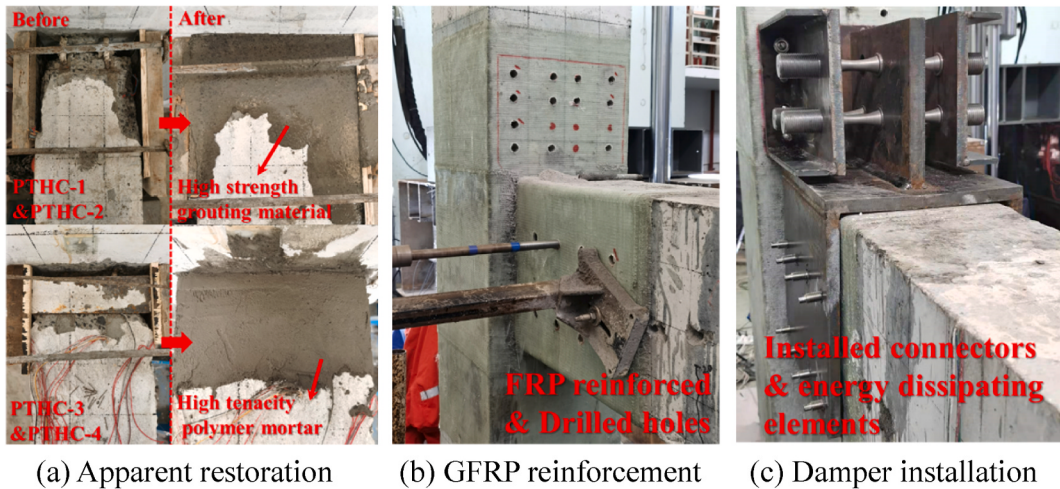


Fig. 4. Reinforcement strategies.

Table 1
Description of specimens.

Specimens	Location of the GFRP arrangement	PT force (kN)	Type of damper	Number of REDEs	Damaged Specimens [49]
RSCPC-1	/	281	Type I	2	PTHC-1
RSCPC-2	Beam end	281	Type I	2	PTHC-2
RSCPC-3	Beam and column ends	281	Type I	1	PTHC-3
RSCPC-3R		361		2	
RSCPC-4	Beam, column ends and core area	281	Type II	2	PTHC-4
RSCPC-4R		361		3	

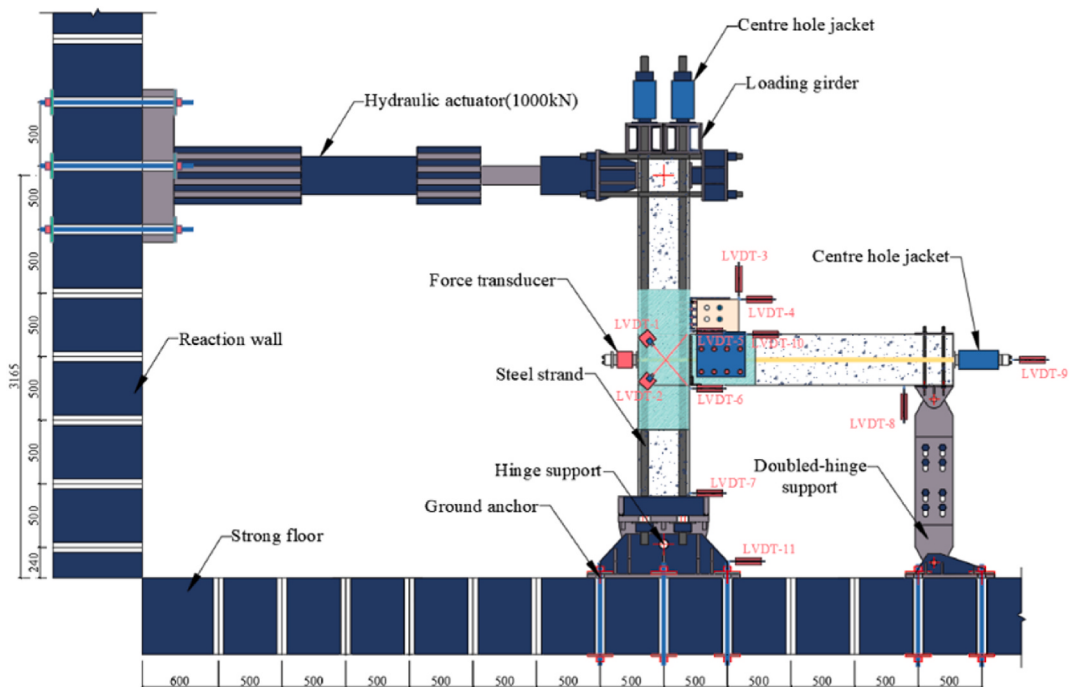


Fig. 5. Test setup for RSCPC specimens.

2.3. Test setup

Fig. 5 shows a schematic of the test setup for the RSCPC specimens. The PC column was restricted with a hinge support at the base, and the beam end farthest from the column was subjected to a doubled-hinge support to simulate the contraflexure point (zero moment). All the bottom supports were connected to a strong floor with ground anchors. The MTS hydraulic actuator with a maximum output force of 1000 kN was connected to the top of the column by four tie rods and was fixed to the reaction wall by anchor rods to apply reverse cyclic loading to the specimens. Four center-hole jacks were installed on top of the column to transfer a constant axial force of 916.80 kN using loading girders and steel strands. The axial compressive ratio μ was approximately 0.30, which was consistent with the axial pressure of the PTHC specimens before seismic damage. In addition, a force transducer with a range of 1000 kN was placed at the end of the column to monitor the change in the PT force during the loading process.

Eleven linear variable displacement transformers (LVDTs) were used to monitor the displacement response of the specimens at various measurement points during loading. Of these, LVDTs-1 and -2 were applied to monitor the deformation of the core area of the beam-to-column connections, LVDTs-3 and -4 were used to monitor the relative horizontal and vertical movement between the damper connectors, and the relative rotation between the beam and column was measured by LVDTs-5 and -6. LVDTs-7 and -11 were used to monitor the slip between the column and strong floor. LVDTs-8 and -9 monitored the vertical and horizontal displacements of the beam end near the double-hinge support, respectively. LVDTs-10 was designed to monitor the slip of the damper connectors.

As shown in Figs. 6 and 15 strain gauges (SGs) were arranged at the REDEs, connectors, and stiffening ribs to monitor the strain changes of the specimens during the experiment. SG-1 to SG-3 were installed on the energy-dissipating element farthest from the center of rotation of the beam, SG-4 to SG-7 were installed on the outside of the connector near the column, and SG-8 and SG-9 were installed on the surface of the stiffener nearest to the connector. SG-10 to SG-15 were installed at the bottom of an internal connector near the beam.

2.4. Loading protocol

A small lateral drift ratio of 0.07 % (approximately 2.0 mm) was applied to verify the operating conditions of the test setup. According to the provisions of ACI374.2R-13 [55], the lateral loading protocol is displacement-controlled loading [56]. Subsequently, the load was applied with three cycles for each stage with drift amplitudes of 0.2 %, 0.25 %, 0.35 %, 0.5 %, 0.75 %, 1 %, 1.5 %, 2 %, 2.75 %, and 3.5 %. If the decrease in the applied load did not exceed 15 % of the ultimate lateral carrying capacity, the drift was increased by 4.25 % and 4.75 % for further loading, as shown in Fig. 7. The loading ended if the force of the connections dropped to 85 % of its maximum force or if there was substantial damage to the REDEs of the damper.

3. Experimental results and discussions

3.1. Failure patterns

The damage developments in the RSCPC specimens during the loading process are shown in Fig. 8. Owing to the different damage states of the hybrid connections and divergent strategies for reinforcement, the failure patterns of each specimen were remarkably different.

For RSCPC-1 and RSCPC-2, the damaged old concrete was retrofitted based on the principles of reduced processes, rapid construction, and restoration of the original form. The failures of the two specimens were mainly attributed to the anchor bolts at the top of the beam and the gap opening between the beam and column surface. In the RSCPC-1 specimen, the first crack developed under loading at a drift of 0.25 % and it was approximately 55 mm from the beam end. As the loading displacement increased, the cracks at the anchor bolt extended toward the beam end by 0.75 % lateral drift ratio, and the cracks extended and penetrated at 1.50 % drift ratio. The concrete was subjected to multidirectional stresses, and three-way cross cracks appeared at the beam end at 2.00 % drift ratio. A large area of concrete became loose and diffused at 3.50 % drift ratio, and eventually, the beam end appeared to drop at 4.25 % drift ratio, as shown in Fig. 8(a). Specimen RSCPC-2 was designed to investigate the restraint effect of GFRP on the earthquake-damaged beam end. The damper was assembled with two REDEs, and the damage condition and GFRP failure mode of the specimen during loading are shown in Fig. 8(b). The GFRP was clearly ruptured at the corner of the beam; at this time, some concrete inside the GFRP was pulled out at 2.75 % drift. As the lateral drift ratio increased to 4.25 %, the GFRP fracture area gradually expanded, and

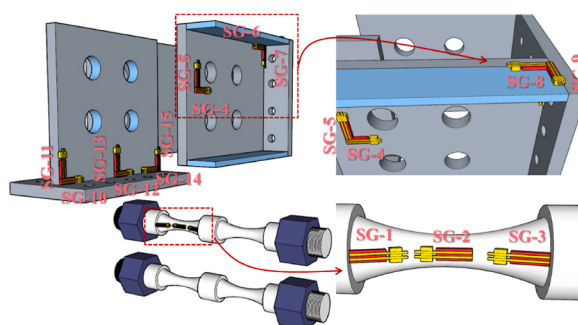


Fig. 6. Arrangement of strain gauges on the damper.

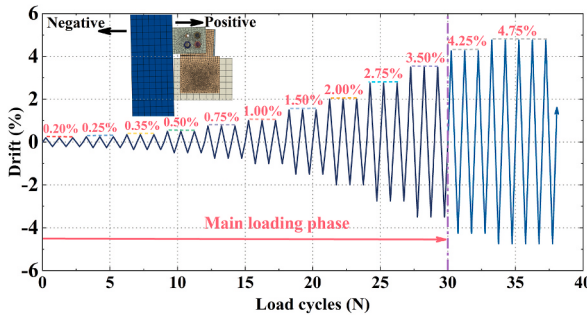


Fig. 7. Loading protocols of experiments.

the internal concrete within the 250 mm from beam end was severely damaged, with the concrete losing its ability to anchor the dampers.

RSCPC-3 had a certain energy-dissipating capacity owing to the residual unbonded bars inside the beam end. Therefore, only one REDE was used, and the initial PT force was maintained at 281 kN, as in the previous specimen. When the lateral drift ratio reached 2.75 %, the REDE produced significant yielding, at which point the maximum displacement of the REDE was approximately 8 mm. At a lateral drift ratio of 3.50 %, the REDE took on an s-shape with a maximum displacement of approximately 18 mm, and the residual reinforcements and REDE were successively damaged at this drift ratio, as shown in Fig. 8(c). The RSCPC-3R supplemented the REDEs while lifting the PT force, and repeated tests were performed. The REDEs exhibited an evident bow-shaped appearance during loading. Similar to RSCPC-1 and RSCPC-2, the GFRP broke and the bolts were pulled out of the beam surface by approximately 5 mm at 3.50 % drift ratio. The residual energy-dissipating bars on the upper part of the beam continuously resisted the concrete in the unbonded section of the beam during the loading process, causing secondary damage, which was particularly evident after RSCPC-3R was disassembled. Owing to the significantly reduced anchoring capacity of the bolts, the residual deformation of the REDEs was large, as shown in Fig. 8(d).

RSCPC-4 had a non-removable connector design that enhances the anchorage of the damper. When the REDEs were damaged, the fractured REDEs were replaced with additional new elements and renumbered as RSCPC-4R. The dampers of these two specimens exhibited good energy-dissipation characteristics, which met the expected requirements of damper ductility and variable damping force, as shown in Fig. 8(e) and (f).

3.2. Load–drift hysteresis curve

The lateral load–drift ratio relationships of the six specimens are shown in Fig. 9. The yield point and maximum force of each specimen are labeled in the diagram, where the yield point is solved using the furthest point method. The yellow curve is the last level of the hysteresis loop for the PTHC specimen, and the green curve is the last level of the hysteresis loop for the first loading of the RSCPC specimen. The hysteresis curves of the six connections showed a flag-shaped shape, which exhibited an evident self-centering feature.

Specimens RSCPC-1 and RSCPC-2 showed similar hysteresis loop shapes despite their envelope areas. At a drift ratio of 3.50 %, the positive and negative maximum forces of RSCPC-1 increased by 7.92 % and 38.08 %, respectively, compared with PTHC-1, and the strength degradation of the hysteresis loop was evident owing to insufficient restraint at the beam end, as shown in Fig. 9(a). The damage to PTHC-2 was almost identical to that of PTHC-1, and the specimen RSCPC-2 after the repair exhibited no significant increase in negative bearing capacity and a positive increase of 24.80 % at a drift ratio of 3.50 %. The dissipated energy of RSCPC-2 at the third loop of 3.50 % drift was 40.17 % higher than that of RSCPC-1, which showed that GFRP restraint at the beam end can effectively improve the energy-dissipation performance of the damper, as shown in Fig. 9(b).

The initial PT force of RSCPC-3 was 281 kN, set at 60 % of the prestress for PTHC-3, and used one REDE for the damper. Two step-downs occurred at 3.5 % drift because of two residual energy-dissipating bars remaining inside PTHC-3. Despite the lower initial PT force, the maximum bearing capacity of RSCPC-3 was almost identical to that of PTHC-3 (the maximum force in positive and negative increased by 1.38 % and 5.01 %, respectively), while the maximum envelope area was increased by 53.89 % at 3.5 % drift ratio, as shown in Fig. 9(c). The initial PT force of RSCPC-3R was 28.50 % higher than that of RSCPC-3, and two REDEs of the damper were replaced. The hysteresis curve envelope area of RSCPC-3R at 3.50 % drift ratio is 86.40 % higher than that of RSCPC-3 in the third loop, as shown in Fig. 9(d).

Owing to the good anchoring of the damper-type-II, the negative energy-dissipating performances of the RSCPC-4 and RSCPC-4R were dramatically improved by the dampers, and the maximum force increased by 104.15 % and 152.32 %, respectively, compared with PTHC-4; no significant strength degradation observed at 4.25 % drift, as shown in Fig. 9(e)–(f).

The comparison of skeleton curves of the RSCPC specimens are shown in Fig. 10. The maximum bearing capacity of RSCPC-2 was 23.95 % higher than that of RSCPC-1, indicating that the use of GFRP restraints can significantly increase the bearing capacity of RSCPC. A comparison of RSCPC-3 and -3R and RSCPC-4 and -4R showed that the addition of REDEs and increased PT force can effectively increase the yield strength and maximum force.

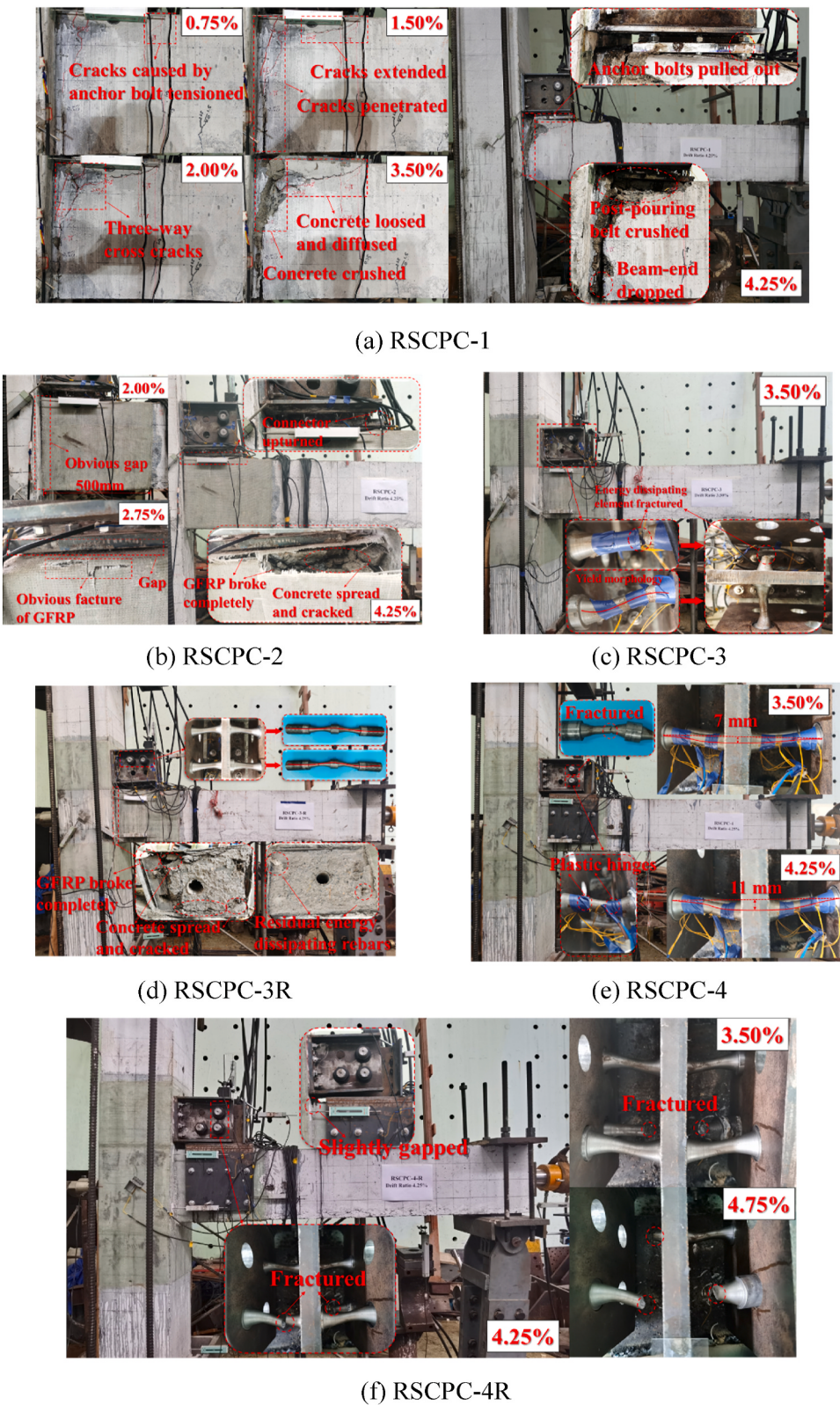


Fig. 8. Failure patterns of the test specimens.

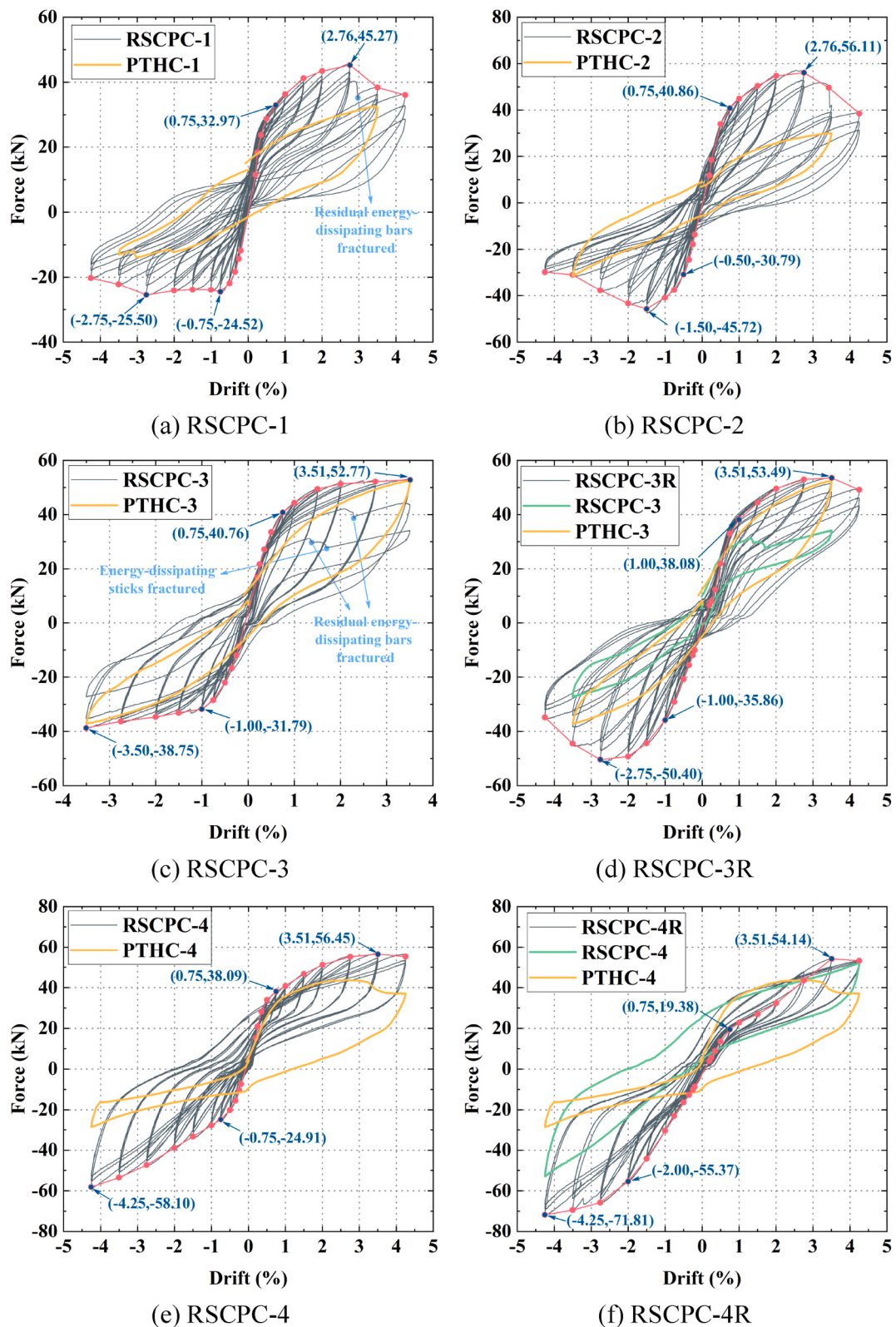


Fig. 9. Hysteresis curves of RSCPCs.

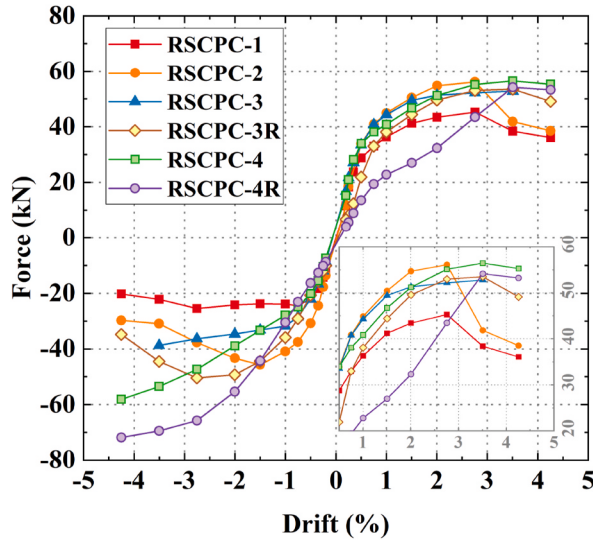


Fig. 10. Envelope curves of RSCPCs.

3.3. Behaviors of PT forces

The PT strands in all the RSCPC specimens remained elastic during the loading process. Owing to damage to the upper part of the beam end, the anchor bolts for the damper connections were pulled out, as shown in Fig. 8(a), (b), and (d). The rotation center of the connection moved downward, and the height of the concrete compression zone decreased. Therefore, the prestressed curve was continuously degraded in the compression direction and was lower than that in the tension direction, as shown in Fig. 11(a), (b), and (d). Owing to the partial adhesion of the GFRP and epoxy resin on the upper part of the beam and the residual mild steel at the base of PTHC-4, the beam-to-column contact surface of RSCPC-4 was not sufficiently open, as shown in Fig. 8(e). GFRP and partially energy-dissipating mild steel limit the gap of connection in the negative direction, which allowed only small growth in the prestress in the tensile direction, and the growth rate of prestress was 33.35 %, whereas it was 66.57 % in the compression direction, as shown in Fig. 11(e). RSCPC-3 and RSCPC-4R exhibited better symmetry of prestress curves and lower damage, with prestress losses of 10.63 % and 11.92 %, respectively, as shown in Fig. 11(c) and (f). Overall, the loss of prestress in all specimens was greater than 10 %, whereas the losses in the PTHC-1 to PTHC-4 were 9.50 %, 7.93 %, 6.33 %, and 8.33 %, respectively. The RSCPC specimens exhibited higher prestress growth rates than the PTHC specimens, but none of the prestressing tendons yielded.

3.4. Stiffness degradation

Stiffness degradation is an important dynamic property of RSCPC specimens and is influenced by concrete damage, the GFRP restraint effect, the number of REDES, and the initial PT force. The secant stiffness values obtained from the hysteresis curves of the specimens were used to evaluate stiffness degradation [57]. The stiffness degradation is expressed as follows:

$$K_{sec\ i} = \frac{|+F_{max\ i}| + |-F_{max\ i}|}{|+U_{max\ i}| + |-U_{max\ i}|} \quad (1)$$

where $+F_{max\ i}$ and $-F_{max\ i}$ are the peak strengths of the i th positive and negative peak points, respectively, and $+U_{max\ i}$ and $-U_{max\ i}$ are the relative displacements of the i th positive and negative peak points, respectively (Fig. 12).

Owing to repeated loading of the specimens, the stiffness of RSCPC-3R and RSCPC-4R remained much lower than the first loading, even with an increased PT force. RSCPC-1 exhibited the lowest overall stiffness owing to the lack of GFRP reinforcement. The initial stiffness of RSCPC-3R was greater than that of RSCPC-4R under higher prestressing; however, RSCPC-4R showed the highest stiffness at 4.25 % drift ratio, which was consistent with the experimental phenomenon, because the damper-type-II did not damage the beam end, and there were few evident cracks in RSCPC-4R. The initial stiffness of RSCPC-3R and -4R decreased significantly after secondary loading; however, the stiffness under a large deformation was not weaker than that under primary loading. Compared with the maximum stiffness, the stiffness of six groups of specimens degraded 74.06 %, 66.17 %, 68.09 %, 42.07 %, 64.06 %, and 36.69 %, respectively, at 2 % drift ratio [58] (compliant with seismic design code in Chinese), as shown in Fig. 12. The stiffness of PTHC-1 to PTHC-4 degraded by 78.21 %, 76.22 %, 72.13 %, and 77.64 % at 2 % drift ratio, respectively. The stiffness degradation rate (SDR) represents the degree of stiffness degradation of the component at a specific drift ratio and is expressed as follows:

$$SDR_i = \frac{Max(K_{sec}) - K_{sec\ i}}{Max(K_{sec})} \quad (2)$$

Compared with PTHC-4, the $SDR_{2\%}$ of RSCPC-4 and -4R were reduced by 17.49 % and 52.74 %, respectively, at 2 % drift ratio, indicating that the proposed repair methods can recover the lost stiffness of PTHCs, and the stiffness of the RSCPCs can be restored by

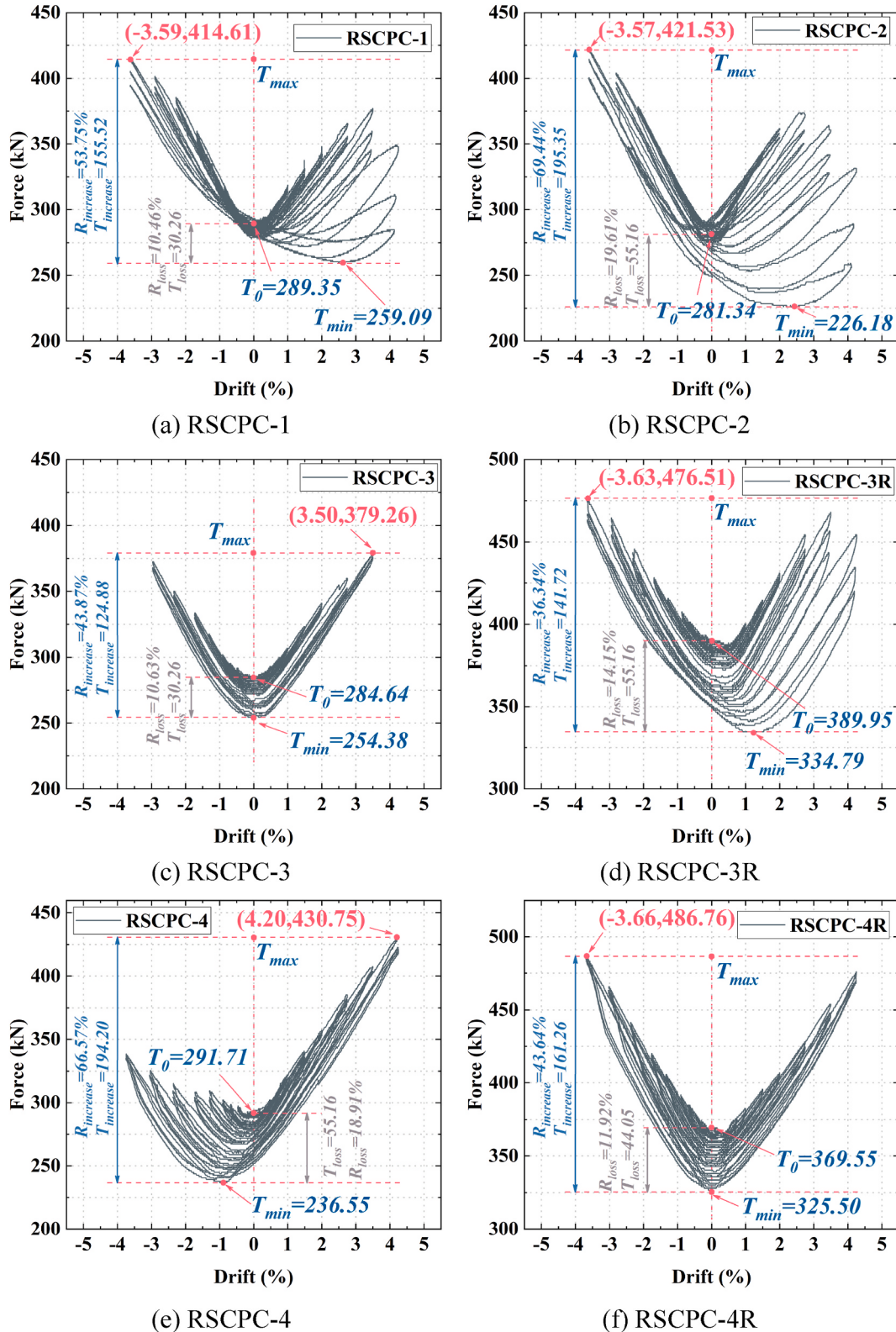


Fig. 11. Tension force versus drift response curves of RSCPCs. Notes: T_0 is the initial prestress, T_{min} is the minimum prestress, T_{max} is the maximum prestress, $T_{increase}$ is the growth value of prestress, $R_{increase}$ is the growth rate of prestress, T_{loss} is the loss value of prestress, R_{loss} is the loss rate of prestress.

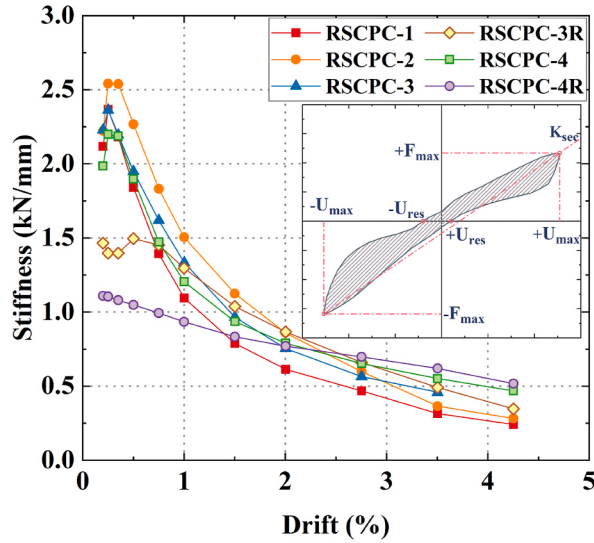


Fig. 12. Lateral stiffness of RSCPCs.

replacing the REDEs under a second rare earthquake.

3.5. Energy-dissipation capacity

The equivalent viscous damping ratio ξ_{ei} , was used to investigate the energy-dissipation capacity of the RSCPCs during the loading process [59], which was calculated by taking the first cycle of each loading level. The calculation formula is as follows:

$$\xi_{ei} = \frac{E_{H,i}}{2\pi \cdot K_{sec,i} \cdot U_{max,i}} \quad (3)$$

$$U_{max,i} = \frac{|+U_{max,i}| + |-U_{max,i}|}{2} \quad (4)$$

where $E_{H,i}$ denotes the envelope area of each hysteretic loop as shown in Fig. 13.

The highest energy-dissipation efficiency was achieved with only one REDE; however, failure occurred before 4.25 % drift ratio. When the number of REDE increased to two, convolved GFRP significantly improved the energy-dissipating capacity, and the maximum equivalent viscous damping coefficient of RSCPC-2 increased by 55.23 % compared to RSCPC-1. Even when the energy-dissipating device was replaced, the equivalent viscous damping ratio of the specimens decreased with repeated loading. The equivalent viscous damping ratios of RSCPC-3R and -4R were reduced by 36.87 % and 15.02 %, respectively, relative to RSCPC-3 and

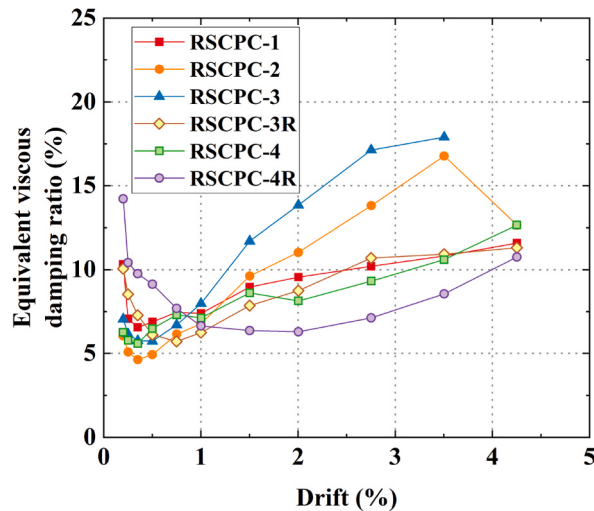


Fig. 13. Equivalent viscous damping ratio curves of RSCPCs.

-4, as shown in Fig. 13.

3.6. Self-centering capability

The self-centering capabilities of the RSCPC were evaluated using the relative self-centering ratio (RSCR) [32], as follows:

$$RSCR_i = 1 - \frac{|+U_{res\ i}| + |-U_{res\ i}|}{|+U_{max\ i}| + |-U_{max\ i}|} \quad (5)$$

where $RSCR_i$ means the self-centering ratio of RSCPC at the i th cycle, $U_{res\ i}$ means the residual drift ratio at the i th cycle, as shown in Fig. 12.

Because of the damage at the beam end, the flexural strength contribution of the damper to the beam end was released, resulting in a sudden increase in the RSCR of RSCPC-1 at 4.25 % drift ratio. The GFRP reinforcement exhibited a boosting effect on the RSCR, especially after 2.75 % drift ratio. RSCPC-3 had the lowest RSCR of 70.06 % because of two residual energy-dissipating rebars within it. With an increase in PT force, the RSCR increased significantly, and the RSCR of RSCPC-4R was 11.05 % higher than that of RSCPC-4. At the same level of design PT force, the RSCR of RSCPC-4R was 10.79 % higher than that of RSCPC-3R, and good anchorage of beam end and damper could also reduce residual deformation, as shown in Fig. 14.

3.7. Strain response

To more accurately determine the strain states of the damper under different deformations, SGs were attached to the REDEs and connectors, as shown in Fig. 6. The maximum strain of the REDEs in the damper and the strain-normalized time histories of RSCPC-3 and RSCPC-4 are shown in Fig. 15. As the ends of the REDEs were not completely fixed, the REDEs rotated during the loading process; therefore, the strain on the SG side did not actually increase. The maximum strain for RSCPC-1 was $4350\ \mu\epsilon$, which is much greater than the nominal yield strain of the REDE (approximately $1119\ \mu\epsilon$), as shown in Fig. 15(a). The REDE of RSCPC-2 reached a strain of $5240\ \mu\epsilon$ after 1.00 % drift ratio, which is much larger than that of RSCPC-1. Therefore, the reinforcement of the beam end was helpful in quickly exerting the energy-dissipation effect of the REDEs, as shown in Fig. 15(b). The maximum strain in the connector was much less than its yield strain, and the REDEs were close to yield at 0.5 % drift ratio, as shown Fig. 15(c). Because of the rotational effect of the REDEs, the true maximum strain for the REDEs could not be monitored, but the strain was greater than those of RSCPC-1 and RSCPC-2, which ensured that the REDEs dissipated energy smoothly, as shown in Fig. 15(d).

4. Recovery force models

The RSCPC system's recovery force mechanism can be derived using the recovery force models for the prefabricated energy-dissipating (PED) and post-tensioned prestressed (PTP) systems [60]. In the following discussion, the recovery force models of PED and PTP were derived in detail through theoretical analyses, and then the key parameters for the recovery model of the RSCPC system were obtained through linear superposition, as shown in Fig. 16. In the following analysis, it will be presumed that the precast beam and column remain elastic.

4.1. Recovery force model of PED system

PED system dissipated seismic energy through plastic deformation of REDEs, so a recovery force model based on energy-dissipating

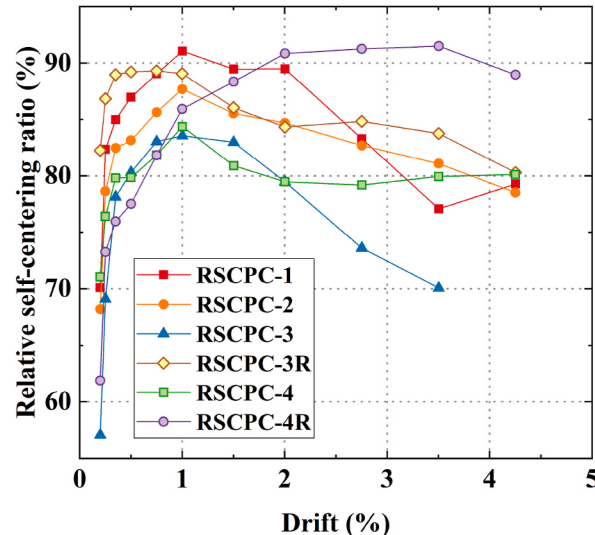


Fig. 14. Relative self-centering ratios of specimens.

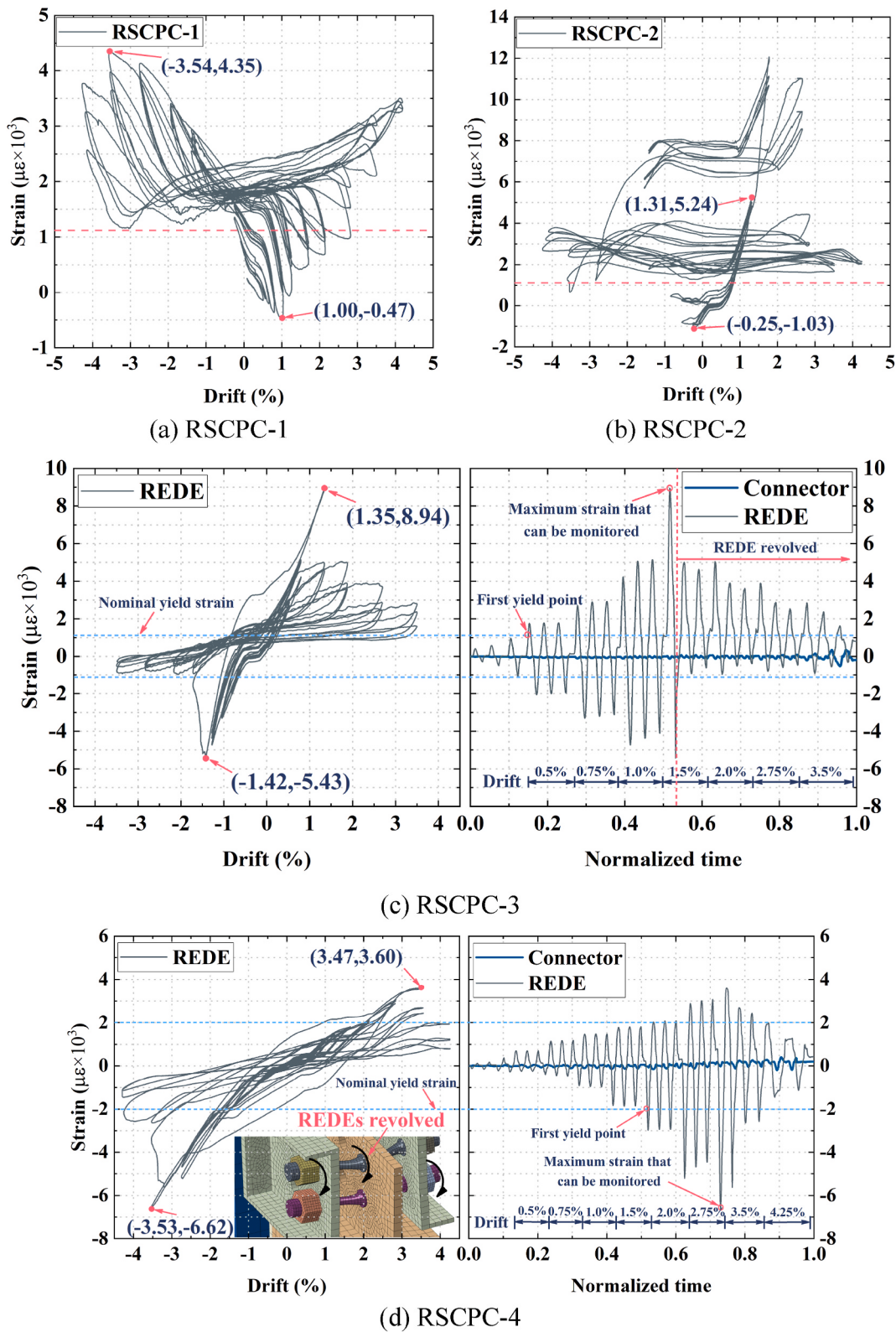


Fig. 15. Strain–drift ratio curves of RSCPCs.

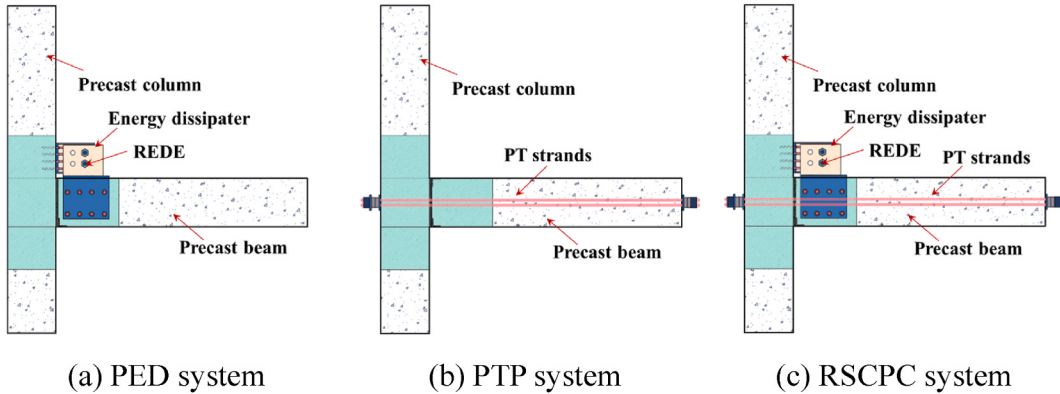


Fig. 16. Analysis model of the individual and integral systems.

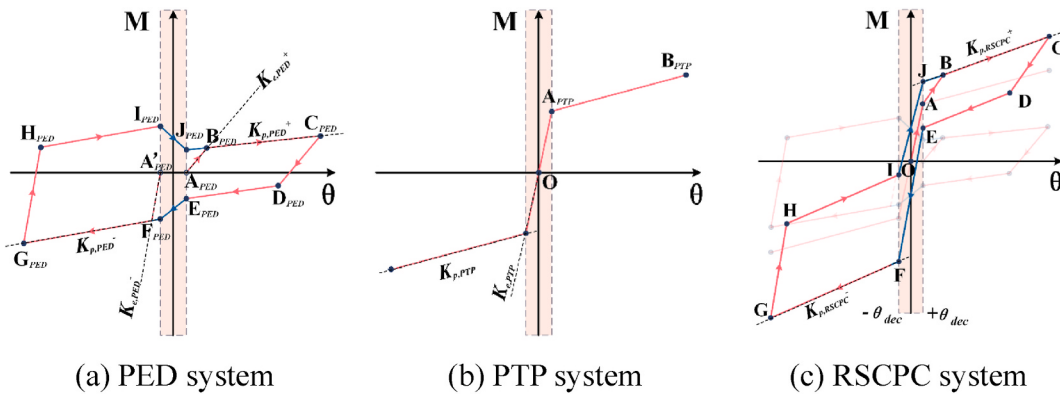


Fig. 17. Recovery force models.

elements and rotation angle was proposed, as shown in Fig. 17(a). When the rotation angle of PED system was less than the decompression drift (θ_{dec}) of the connection, the REDEs did not enter the working state. As the connection completed its decompression state, the gap of the contact surface of beam and column gradually opened, and the PED system entered the elastic deformation state until yield ($A_{PED}-B_{PED}$). It was assumed that the rotation centers of the PED systems change linearly asymptotically, so the bending moment of the beam end of the connection in the stage ($I_{PED}-J_{PED}$, $E_{PED}-F_{PED}$) of decompression drifts presented a linear increase or decrease.

The basic geometry of the REDE is shown in Fig. 18. When the energy-dissipating element is subjected to horizontal force, the REDE produced both bending and shear deformation. When both ends of the steel rod were completely constrained, the REDE can be simplified into an equivalent beam model with fixed ends. Under the given loading conditions, the beam will undergo hyperbolic deformation, and the bending moment increased linearly from the middle of the REDE to the fixed end [61]. The bending moment at position x is as follows:

$$M_x = \frac{2M_1 x}{h} = P \cdot x \quad (5a)$$

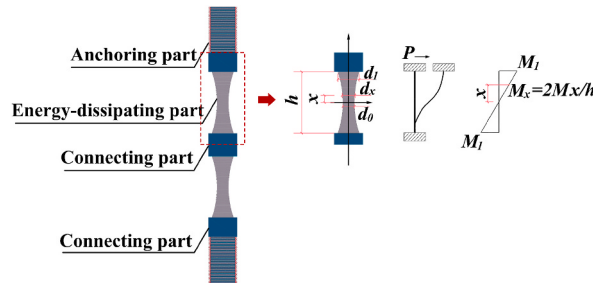


Fig. 18. Equivalent beam model.

Where M_1 is the theoretical maximum bending moment at the end of the REDE, h is the height of the of the REDE, and P is the horizontal load. The plastic bending moment at position x can be calculated by Eqs. (6) and (7):

$$M_{p,x} = F_y \cdot \gamma_x = F_y d_x^3 / 6 \quad (6)$$

$$d_x = (6P/F_y)^{1/3} \cdot \sqrt[3]{x} \quad (7)$$

Where F_y is the yield stress of the steel, γ_x is the modulus of the plastic section, and d_x is the diameter of the REDE at position x .

The strength of a damper dominated by bending deformation can be calculated by the plastic moment on any section of an ideal shape [62]. According to the section of the fixed end, the bending moment is calculated as Eq. (8).

$$M_p = F_y \cdot \gamma = F_y d_1^3 / 6 \quad (8)$$

The plastic strength (P_p) is the horizontal load when the bending moment at both ends of the REDE is equal to M_p . The yield strength (P_y) can be solved by using the plastic development coefficient on the basis of the plastic strength.

$$P_p = F_y d_1^3 / 3h \quad (9)$$

$$P_y = F_y d_1^3 / 5.1h \quad (10)$$

According to the principle of virtual work, the elastic stiffness (K_e) and yield displacement (δ_y) can be calculated. In a system subjected to a virtual unit horizontal force, when the maximum bending moment acting on both ends is m , the virtual bending moment at position x (m_x) is $2mx/h$. If the virtual external work is equal to the virtual internal work, the equation for the relative displacement (δ) is:

$$1 \bullet \delta = \int_{-\frac{h}{2}}^{\frac{h}{2}} \frac{M_x m_x}{EI_x} dx = \frac{512M_1 m}{\pi Eh^2} \int_0^{\frac{h}{2}} \frac{x^2}{d_x^4} dx = \frac{128P}{\pi E} \int_0^{\frac{h}{2}} \frac{x^2}{d_x^4} dx \quad (11)$$

where E is the elasticity modulus and I_x is the moment of inertia of the REDE at position x . When the actual fixity at the ends is considered, K_e can be expressed as:

$$K_e = c \bullet \frac{P}{\delta} = \frac{c \bullet \pi E}{128 \int_0^{\frac{h}{2}} \frac{x^2}{d_x^4} dx} \quad (12)$$

$$d_x = 2 \left(\frac{d_1^2 - d_0^2 + h^2}{4(d_1 - d_0)} - \sqrt{R^2 - x^2} \right) \quad (13)$$

$$R = \frac{(d_1 - d_0)^2 + h^2}{4(d_1 - d_0)} \quad (14)$$

where c is the stiffness coefficient, which is the reduced ratio compared to the value for fixed-fixed ends, with a value of 1.0 or less, and

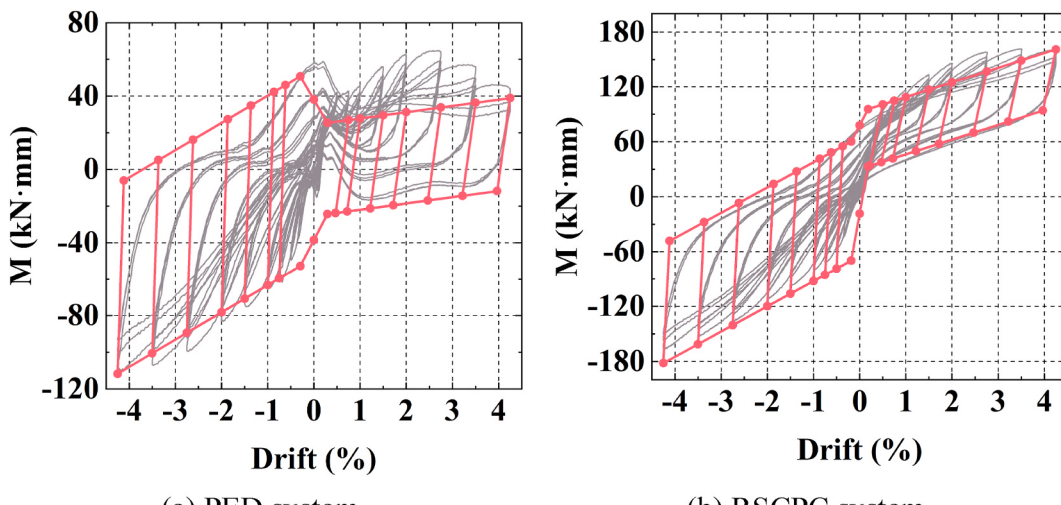


Fig. 19. Comparisons of theoretical recovery force models and hysteresis curves.

δ_y is calculated as Eq. (15).

$$\delta_y = \frac{1}{c} \bullet \frac{P_y}{K_e} = \frac{1}{c} \bullet \frac{F_y d_1^3}{5.1 h} \bullet \frac{\int_0^{\frac{h}{2}} (x^2/d_x^4) dx}{\pi E} \quad (15)$$

In this paper, the δ_y of a single REDE is calculated to be 0.41 mm, and the K_e is 129.82 kN/mm. According to the principle of rigid body kinematics, the $K_{e,PED}^+$ of beam end of RSCPC-4 with two REDEs under PED system is 180.40 kN/mm, and the $K_{e,PED}^-$ is 786.89 kN/mm. The $K_{p,PED}^+$ of PED system is calculated to be 3.41 kN/mm and $K_{p,PED}^-$ is 14.89 kN/mm. The comparison between the theoretical recovery force model of PED system and hysteresis curve measured by experiment is shown in Fig. 19(a). Since the constitutive material of REDEs is assumed to be a bilinear hysteresis model, the strengthening phenomenon of steel is ignored. Considering the error caused by the test itself, there is a certain difference between the hysteresis model in the positive direction, but the negative is in good agreement.

4.2. Recovery force model of PTP system

In the PTP system, the PT strands remain elastic throughout the calculation, and the typical drift-moment curve of the PTP system is shown in Fig. 17(b). Before the contact surface of the precast beam and column is opened, the beam will appear a small elastic deformation. Before the rotational angle reaches the decompression drift θ_{dec} , the rotational stiffness of the PTP system is $K_{e,PTP}$, and the initial prestress is F_{IPT} . When the drift reaches θ_{dec} , the rotational stiffness of the PTP system is $K_{p,PTP}$, and the pure PTP system has no energy dissipation capacity.

Under the action of initial prestress, the beam ends as well as the column surface are tightly fitted, as the Angle increases, the PTP system join the decompression stage and finally open the contact surface. The bending moment (M_{dec}) of PTP system at the θ_{dec} can be calculated by the following formula:

$$M_{dec} = F_{PT} \cdot \frac{H_{beam}}{2} \quad (16)$$

$$\theta_{dec} = \frac{M_{dec} \cdot L_{beam}}{3E_c I'_{beam}} \quad (17)$$

where L_{beam} is the distance from the contact surface of the beam end to the support, E_c is the elastic modulus of concrete, and $E_c I'_{beam}$ is the effective stiffness of the beam.

In the PTP system, with the opening of the gap, the beam will have a certain amount of compression in the axial direction due to the effect of prestressing, which is Δ_{beam} , and the axial force growth of the beam end in the PTP system is actually equal to the growth of prestressing, so the following equation can be established:

$$K_{PT} \cdot (\Delta_{PT} - \Delta_{beam}) = K_{beam} \cdot \Delta_{beam} \quad (18)$$

where K_{PT} is the axial stiffness of PT strands, Δ_{PT} is the axial elongation of PT strands, Δ_{beam} is the axial compression of PT strands, and K_{beam} is the stiffness of beam along the axis direction.

The relationship between the elongation of PT strands and the axial compression of beam is as follows:

$$\Delta_{PT} = \frac{H_{beam}}{2} \cdot \theta \quad (19)$$

$$\Delta_{beam} = \frac{K_{PT} \cdot \Delta_{PT}}{K_{beam} + K_{PT}} \quad (20)$$

and the K_{PT} and K_{beam} can be calculated by Eqs. (21) and (22):

$$K_{PT} = \frac{E_{PT} \cdot A_{PT}}{L_{PT}} \quad (21)$$

$$K_{beam} = \frac{E_c \cdot A_{beam}}{L_{beam}} \quad (22)$$

where E_{PT} is the elastic modulus of the PT strands, A_{PT} is the equivalent area of the PT strands, L_{PT} is the unbonded length of the PT strands, and A_{beam} is the equivalent area of the section of the precast beam.

When the actual opening gap of PTP system is θ_{AR} , the resultant force F_{RPT} of PT strands is calculated as Eq. (23):

$$F_{RPT} = F_{IPT} + K_{PT} \cdot (\Delta_{PT} - \Delta_{beam}) = F_{IPT} + K_{PT} \cdot \left(\Delta_{PT} - \frac{K_{PT} \cdot \Delta_{PT}}{K_{beam} + K_{PT}} \right) = F_{IPT} + K_{PT} \theta_{AR} \left(1 - \frac{K_{PT}}{K_{beam} + K_{PT}} \right) \frac{H_{beam}}{2} \quad (23)$$

the contribution of PT strands to the beam end bending moment of PTP system is calculated Eqs. (24) and (25):

$$M_{PTP} = F_{RPT} \cdot \frac{H_{beam}}{2} = F_{IPT} \frac{H_{beam}}{2} + K_{p,PTP} (\theta - \theta_{e,PTP}) \quad (24)$$

$$K_{p,PTP} = \frac{H_{beam}}{2} \cdot K_{PT} \cdot \left(\frac{H_{beam}}{2} - \frac{K_{PT}}{K_{beam} + K_{PT}} \cdot \frac{H_{beam}}{2} \right) \quad (25)$$

4.3. Recovery force model of RSCPC system

As shown in Fig. 17(c), the recovery force model of the RSCPC system can be obtained by linear superposition of the PED system and PTP system. The comparison between the theoretical recovery force model of RSCPC system and hysteresis curve measured by experiment is shown in Fig. 19(b). In this paper, θ_{dec} is calculated as 0.18 %, $K_{p,RSCPC}^+$ is 16.08 kN/mm and $K_{p,RSCPC}^-$ is 27.56 kN/mm.

5. Conclusions

This study developed a novel repair method for earthquake-damaged hybrid connections. Four damaged PTHCs were repaired and reinforced, and low-cycle reciprocating tests of the reinforced specimens were performed on this basis. The hysteresis properties of PTHCs and RSCPCs and the mechanical behaviors of RSCPCs with different reinforcement strategies were compared. The main conclusions of this study are as follows:

- (1) All the RSCPC specimens exhibited a significant improvement in both energy-dissipation and bearing capacity compared to the last stage of the hysteresis loop of the PTHCs. The initial prestress of RSCPC-3R was 11.10 % less than the final prestress of PTHC-3. However, the bearing capacity was 22.59 % higher than the original specimen, and the energy dissipation increased by 0.74 % at 3.50 % drift ratio. With reasonable reinforcing, the hysteresis performance of the reinforced connections was close to that of the PTHCs.
- (2) The form of connections between the damper and beam exhibited significant influence on the bearing capacity and ductility of the RSCPCs. Embedding anchor bolts in the upper part of the beam to connect the damper would cause the concrete to crack under the action of multidirectional stress, and the bearing capacity of the connections would degenerate too quickly under a large drift ratio. The use of damper-type-II allowed the energy dissipation of the REDEs to be fully utilized. The number of REDEs and connector forms should be reasonably designed according to the damage level of the PTHCs.
- (3) The GFRP constraint at the beam end can effectively improve the seismic damage caused by multiple rare earthquakes. The damage at the beam end causes the position of the beam to shift under a reciprocating load, thus increasing the loss of prestress. The improved constraint effect of the beam end was also beneficial to the energy-dissipation capacity of the damper, thus increasing the equivalent viscous damping ratio of the connections.
- (4) The stiffness of the RSCPC specimens could be restored by replacing the REDEs; but the initial stiffness at each time was not as good as that of the first loading specimens such as RSCPC-3 and -3R and RSCPC-4 and -4R. However, as the drift increased, the stiffness degradation of the specimens with more REDEs was smoother, and the final stiffness was larger than that of specimens with fewer REDEs. Compared to PTHC-1, PTHC-2, PTHC-3, and PTHC-4, the SDRs of RSCPC-1, RSCPC-2, RSCPC-3, and RSCPC-4 decreased by 5.31 %, 13.19 %, 5.60 %, and 17.49 %, respectively, at 2 % drift ratio. This indicates that this repair method can realize stiffness recovery of earthquake-damaged connections.
- (5) The results obtained through the recovery force model introduced in this research exhibit a satisfactory correlation with the experimental data, which indicates that the model can accurately anticipate the hysteresis behavior of RSCPCs, and can be used for the design of such connections in subsequent projects.

It should be noted that the proposed recovery force model is effective in predicting the hysteresis behavior of the RSCPC system; however, the influence of concrete plasticity and damage on the bearing capacity degradation of the connections is not considered. Therefore, a more universal analytical model of the RSCPC system still need further study.

CRediT authorship contribution statement

Tianyang Zhang: Investigation, Software, Formal analysis curation, Data curation, Writing - original draft, Writing - Review & Editing. Weizhi Xu: Conceptualization, Methodology, Funding acquisition, Writing - original draft, Writing-review & editing. Shuguang Wang: Software, Validation, Formal analysis, Investigation, Writing - review & editing. Dongsheng Du: Investigation, Writing - review & editing. Linlin Xie: Funding acquisition, Writing - review & editing. Qisong Miao: Supervision, Writing - review & editing.

Declaration of competing interest

We declare that we have no financial and personal relationships with other people or organizations that can inappropriately influence our work, there is no professional or other personal interest of any nature or kind in any product, service and/or company that could be construed as influencing the position presented in, or the review of, the manuscript entitled "Seismic behavior of earthquake-damaged hybrid connections reinforced with replaceable energy-dissipating elements".

Data availability

Data will be made available on request.

Acknowledgments

The authors are greatly thankful for the financial support from the National Natural Science Foundation of China (52208173), Fellowship of China Postdoctoral Science Foundation (2022M721591) and Scientific Research Fund of Multi-Functional Shaking Tables Laboratory of Beijing University of Civil Engineering and Architecture (2022MFSTL03). The authors are also grateful for the support received from Jiangsu Funding Program for Excellent Postdoctoral Talent.

References

- [1] S. Li, Z.X. Zuo, C.H. Zhai, S.Y. Xu, L.L. Xie, Shaking table test on the collapse process of a three-story reinforced concrete frame structure, *Eng. Struct.* 118 (2016) 156–166.
- [2] M.S. Gong, Z.X. Zuo, X.M. Wang, X.T. Lu, L.L. Xie, Comparing seismic performances of pilotis and bare RC frame structures by shaking table tests, *Eng. Struct.* 199 (2019), 109442.
- [3] Z.P. Chen, D.C. Feng, K.J. Ma, G. Wu, Shaking table test and evaluation of a novel high-rise large span concrete cassette structure, *Eng. Struct.* 238 (2021), 112205.
- [4] B. Zhao, F. Taucer, T. Rossetto, Field investigation on the performance of building structures during the 12 May 2008 Wenchuan earthquake in China, *Eng. Struct.* 31 (2009) 1707–1723.
- [5] A.S. Elnashai, B. Gencturk, O.S. Kwon, Y.M.A. Hashash, S.J. Kim, S.H. Jeong, The Maule (Chile) earthquake of February 27, 2010: development of hazard, site specific ground motions and back-analysis of structures, *Soil Dynam. Earthq. Eng.* 42 (2012) 229–245.
- [6] K. Sharma, L. Deng, C.C. Noguez, Field investigation on the performance of building structures during the April 25, 2015, Gorkha earthquake in Nepal, *Eng. Struct.* 121 (2016) 61–74.
- [7] M.J.N. Priestley, Overview of PRESSS research program, *PCI J.* 36 (1991) 50–57.
- [8] J.F. Stanton, N.M. Hawkins, T.R. Hicks, PRESSS project 1.3-connection classification and evaluation, *PCI J.* 36 (6) (1991) 62–71.
- [9] G.S. Cheok, H.S. Lew, Model precast concrete beam-to-column connections subject to cyclic loading, *PCI J.* 38 (4) (1993) 80–92.
- [10] G. Song, T.Y. Yang, Y. Zhou, Distribution of hysteretic energy demands in self-centering concrete frames with hybrid joints, *Soil Dynam. Earthq. Eng.* 148 (2021), 106828.
- [11] B.X. Song, W.Z. Xu, D.S. Du, S.G. Wang, Quantification of moment–rotation relationship of monolithic precast beam–column connections, *Buildings* 12 (2021) 1–11.
- [12] B.X. Song, W.Z. Xu, D.S. Du, S.G. Wang, W.W. Li, Y.L. Zhang, Seismic design of hybrid unbonded post-tensioned precast concrete joints based on bearing capacity and energy dissipation capacity, *Adv. Struct. Eng.* 21 (2020) 1724–1738.
- [13] G.S. Cheok, W.C. Stone, S.D. Nakaki, Simplified Design Procedure for Hybrid Precast Concrete Connections, Report NISTIR 5765: National Institute of Strands and Technology, 1996.
- [14] L. Palmieri, E. Saqan, C. French, M. Kreger, Ductile Connections for Precast Concrete Frame Systems, ASCE, 1996.
- [15] W.C. Stone, G.S. Cheok, J.F. Stanton, Performance of hybrid moment-resisting precast beam-column concrete connections subjected to cyclic loading, *ACI Struct. J.* 91 (1995) 229–249.
- [16] G.S. Cheok, W.C. Stone, Performance of 1/3 Scale Model Precast Concrete Beam-Column Connection Subject to Cyclic Inelastic Loads, Report NISTIR 5436: National Institute of Strands and Technology, 1994.
- [17] J. Stanton, W.C. Stone, G.S. Cheok, A hybrid reinforced precast frame for seismic regions, *PCI J.* 42 (2) (1997) 20–32.
- [18] M.J.N. Priestley, S. Sritharan, J.R. Conley, S. Pampanin, Preliminary results and conclusions from the PRESSS five-story precast concrete test building, *PCI J.* 44 (6) (1999) 42–67.
- [19] S. Ozden, O. Ertas, Behavior of unbonded, post-tensioned precast concrete connections with different percentages of mild steel reinforcement, *PCI J.* 52 (2) (2007) 32–44.
- [20] B.G. Morgen, Y.C. Kurama, A friction damper for post-tensioned precast concrete moment frames, *PCI J.* 24 (49) (2004) 112–123.
- [21] B.G. Morgen, Y.C. Kurama, Seismic design of friction-damped precast concrete frame structures, *J. Struct. Eng.* 133 (11) (2007) 1501–1511.
- [22] K. Takeaki, Moment and energy dissipation capacities of post-tensioned precast concrete connections employing a friction device, *Eng. Struct.* 138 (1) (2007) 170–180.
- [23] R.J. Mitran, An Ounce of Prevention: Probabilistic Loss Estimation for Performance-Based Earthquake Engineering, California Institute of Technology, 2007. Ph.D. Dissertation.
- [24] H.J. Jiang, H.F. Bu, L.S. He, A new method for function-loss based seismic resilience assessment of buildings, *Eng. Struct.* 266 (2022), 114613.
- [25] L.J. Huang, Z. Zhou, Y. Wei, Q. Xie, X.Y. Sun, Seismic performance and resilience assessment of friction damped self-centering prestressed concrete frames, *Eng. Struct.* 263 (2022), 114346.
- [26] T. You, W. Wang, S. Tesfamariam, Effects of self-centering structural systems on regional seismic resilience, *Eng. Struct.* 274 (2023), 115125.
- [27] L.J. Huang, Z. Zhou, X.G. Huang, Y.W. Wang, Variable friction damped self-centering precast concrete beam–column connections with hidden corbels: experimental investigation and theoretical analysis, *Eng. Struct.* 206 (2020), 110150.
- [28] L.J. Huang, B. Zeng, Z. Zhou, W.Q. Zhang, Y. Wei, C.Y. Li, Seismic behavior and reliability of variable friction damped self-centering prestressed concrete frames considering bolt bearing, *Soil Dynam. Earthq. Eng.* 164 (2023), 107643.
- [29] X.N. Cai, Z.F. Pan, Y.Z. Zhu, N.N. Gong, Y.W. Wang, Experimental and numerical investigations of self-centering post-tensioned precast beam-to-column connections with steel top and seat angles, *Eng. Struct.* 226 (2021), 111397.
- [30] F.F. Geng, Y.L. Ding, H.L. Wu, J.P. Yang, W. Shen, Seismic performance enhancing of novel self-centering precast concrete frame using replaceable hysteretic dampers, *J. Build. Eng.* 42 (2021), 103059.
- [31] W.C. Xue, X.Y. Hu, L.J. Dai, B. Zhu, Cyclic behavior of semi-rigid precast concrete beam-to-column subassemblages with rapid assembly connections, *J. Build. Eng.* 46 (2022), 103671.
- [32] L.H. Zhu, Q.J. Ning, W. Han, C. Zhao, Seismic performance of self-centering concrete-filled square steel tubular column-to-steel beam connection equipped with SMA bolts, *Thin-Walled Struct.* 183 (2023), 110351.
- [33] H.S. Wang, E.M. Marino, P. Pan, H. Liu, X. Nie, Experimental study of a novel precast prestressed reinforced concrete beam-to-column joint, *Eng. Struct.* 156 (2008) 68–81.
- [34] C.L. Wang, Y. Liu, X.L. Zheng, J. Wu, Experimental investigation of a precast concrete connection with all-steel bamboo-shaped energy dissipaters, *Eng. Struct.* 178 (2019) 298–308.
- [35] Z.H. Li, Y.H. Qi, J. Teng, Experimental investigation of prefabricated beam-to-column steel joints for precast concrete structures under cyclic loading, *Eng. Struct.* 209 (15) (2020), 110217.
- [36] W. Huang, G.X. Hu, X.W. Miao, Z.H. Fan, Seismic performance analysis of a novel demountable precast concrete beam-column connection with multi-slit devices, *J. Build. Eng.* 44 (2021), 102663.
- [37] Y.D. Li, F.F. Geng, Y.L. Ding, L.B. Wang, Experimental and numerical study of low-damage self-centering precast concrete frame connections with replaceable dampers, *Eng. Struct.* 220 (2020), 111011.
- [38] Y.D. Li, F.F. Geng, Y.L. Ding, L.B. Wang, Influence of mild steel damper design parameters on energy dissipation performance of low-damage self-centering precast concrete frame connections, *Soil Dynam. Earthq. Eng.* 144 (2021), 106696.
- [39] Y. Liu, W.Y. Wang, Concept and analysis of a low-cost energy dissipater with partially self-centering mechanism, *J. Build. Eng.* 44 (2021), 102881.

- [40] H.S. Wang, E.M. Marino, P. Pan, Design, testing and finite element analysis of an improved precast prestressed beam-to-column joint, *Eng. Struct.* 199 (19) (2019), 109661.
- [41] H.S. Wang, F. Barbagallo, P. Pan, Test of precast pre-stressed beam-to-column joint with damage-free reinforced concrete slab, *Eng. Struct.* 210 (2020), 110368.
- [42] H.S. Wang, F. Barbagallo, E.M. Marino, P. Pan, Optimal design of the connection between RC slab and precast pre-stressed beam to column joint, *Eng. Struct.* 270 (2020), 114893.
- [43] S. Pampanin, M.J.N. Priestley, S. Sritharan, Analytical modelling of the seismic behaviour of precast concrete frames designed with ductile conn., *J. Earthq. Eng.* 5 (2001) 329–367.
- [44] T. Smith, F.C. Ponzo, A.D. Cesare, S. Pampanin, D.M. Carradine, A.H. Buchanan, D. Nigro, Post-tensioned glulam beam-column joints with advanced damping systems: testing and numerical analysis, *J. Earthq. Eng.* 18 (2014) 147–167.
- [45] M. Newcombe, S. Pampanin, A. Buchanan, A. Palermo, Section analysis and cyclic behavior of post-tensioned jointed ductile connections for multi-story timber buildings, *J. Earthq. Eng.* 12 (2008) 83–110.
- [46] F. Sarti, A. Palermo, S. Pampanin, Quasi-static cyclic testing of two-thirds scale unbonded posttensioned rocking dissipative timber walls, *J. Earthq. Eng.* 142 (2015), E4015005.
- [47] A. Iqbal, S. Pampanin, A. Palermo, A. Buchanan, Seismic performance of full-scale post-tensioned timber beam-column joints, *J. Earthq. Eng.* 20 (2016) 383–405.
- [48] D.J. Shen, M. Li, C. Liu, J.C. Kang, C.C. Li, J. Yang, Seismic performance of corroded reinforced concrete beam-column joints repaired with BFRP sheets, *Construct. Build. Mater.* 307 (8) (2021), 124731.
- [49] Z.M. Jalaeian, H. Shariatmadar, Repair and retrofitting of external RC beam-to-column joints using the hybrid NSM + EBR method, *Eng. Struct.* 263 (15) (2022), 114370.
- [50] F. Faleschini, L.J. Gonzalez, M.A. Zanini, L. Hofer, L. Snead, C. Pellegrino, Repair of severely-damaged RC exterior beam-column joints with FRP and FRCM composites, *Compos. Struct.* 207 (2019) 352–363.
- [51] D.J. Shen, M. Li, Q. Yang, C.Y. Wen, C. Liu, J.C. Kang, Seismic performance of earthquake-damaged corroded reinforced concrete beam-column joints retrofitted with basalt fiber-reinforced polymer sheets, *Struct. Infrastruct. Eng.* (2022) 1–17.
- [52] Q. Zhang, Z.Y. Wei, X.L. Gu, Q.C. Yang, S.Y. Li, Y.S. Zhao, Confinement behavior and stress-strain response of square concrete columns strengthened with carbon textile reinforced concrete (CTRC) composites, *Eng. Struct.* 266 (2022), 114592.
- [53] Q. Zhang, N.H. Zheng, X.L. Gu, Z.Y. Wei, Z. Zhang, Study of the confinement performance and stress-strain response of RC columns with corroded stirrups, *Eng. Struct.* 266 (2022), 114476.
- [54] S.G. Wang, T.Y. Zhang, W.Z. Xu, D.S. Du, Y.L. Zhang, Experimental and numerical investigations on novel post-tensioned precast beam-to-column energy-dissipating connections, *Structures* 24 (2023) 117–133.
- [55] ACI Committee 374, Guide for Testing Reinforced Concrete Structural Elements under Slowly Applied Simulated Seismic Loads (374.2 R-13), ACI, Farmington Hills (MI), 2013.
- [56] J.J. Fan, G. Wu, D.C. Feng, Y.H. Zeng, Y. Lu, Seismic performance of a novel self-sustaining beam-column connection for precast concrete moment-resisting frames, *Eng. Struct.* 222 (2020), 111096.
- [57] W.Z. Xu, T.Y. Zhang, X. Chen, Q.S. Miao, S.G. Wang, D.S. Du, Experimental and numerical investigation on the seismic performance of masonry walls reinforced by PC panels, *J. Build. Eng.* 58 (2022), 105049.
- [58] GB50010-2010, Code for Design of Concrete Structures, China Construction Industry Press, Beijing, China, 2010 (in Chinese).
- [59] H.H. Ghayeb, R.H. Abdul, S.N.H. Ramli, Seismic performance of innovative hybrid precast reinforced concrete beam-to-column connections, *Eng. Struct.* 202 (2020), 109886.
- [60] Y. Chen, C. Chen, C. Chen, Study on seismic performance of prefabricated self-centering beam to column rotation friction energy dissipation connection, *Eng. Struct.* 241 (2021), 112136.
- [61] H.L. Chang, K.J. Young, K.M. Jeong, H.L. Seung, D.K. Sang, Non-uniform steel strip dampers subjected to cyclic loadings, *Eng. Struct.* 99 (2015) 192–204.
- [62] A.A. Hosseini, P.N. Esmaeil, E.E. Homayoon, Experimental and analytical study of block slit damper, *J. Constr. Steel Res.* 141 (2018) 167–178.